A universal relative density equation: exploring the physical mechanism of laser powder bed fusion entrained porosity

Xianmeng Tu[1], Jialong Chen[1], Xiaoyuan Ji[1,*], Huanqing Yang[2], Huatang Cao[1], Guomin Le[3], Shengzhi Zhou[1], Dongjian Peng[2], Zeming Wang[1,4], Yajun Yin[1], Zejun Zhang[1], Yanyuan Zhou[5], Menghuai Wu[6], Jianxin Zhou[1,*]

1. State Key Laboratory of Materials Processing and Die & Mould Technology, School of Materials Science and Engineering, Huazhong University of Science and Technology, Wuhan, Hubei, 430074, China

2. Xi'an Spac d Porositye Engine Co., Ltd., Xi'an, 710100, China

3. Material Research Institute, China Academy of Engineering Physics, Mianyang, Sichuan, 621900, China

4. Nuclear Power Institute of China, Chengdu, Sichuan, 610005, China

5. Ningbo Institute of Materials Technology and Engineering, Chinese Academy of Sciences, Ningbo, Zhejiang 315201, China

6. Department of Metallurgy, University of Leoben, A-8700 Leoben, Austria

Corresponding author e-mail: jixiaoyuan@hust.edu.cn (Xiaoyuan Ji); zhoujianxin@hust.edu.cn (Jianxin Zhou)

Abstract: Whether an interpretable universal relative density equation can be established for laser powder bed fusion (LPBF) forming applicable to multiple metals is a highly challenging task and crucial for exploring the physical mechanism of density and forming high-quality components. Previous studies have investigated the relationship between process parameters and density, but cannot uncover its intrinsic mechanism. Here, a global, stepwise, centrally dense hexagonal design of experiments is applied to the additive manufacture of 65 GH4169 nickel superalloy materials each employing different laser processing conditions; Inspiring from Morse potential energy function, the relationship between laser energy density (E) and relative density is fitted by the Box Lucas equation; Finally, the universal relative density equation is constructed using Data-physics fusion driven (DPFD) approach by introducing contact angle (θ) and boiling factor (b). The results illustrate that the relative density increases rapidly as E increases in the low E regime, but it falls slowly as E exceeds the optimal range (process window); Meanwhile, the density rapidly increases as θ decreases in the low E regime, but it falls slowly as b increase when E exceeds the optimal process window. The accuracy and predictability of the unified density equation were verified by 9 grades and 275 data pairs points, and validated by 10000 sets of stepwise regression model prediction data. This progress breaks through the limitations of P-V space design. It provides theoretical guidance and a simple basic technical choice for exploring the production of fully dense products for LPBF production.

Keywords: Relative density equation, Laser powder bed fusion (LPBF), Physical mechanism, GH4169 superalloy, Data-physics fusion driven (DPFD).

1 Introduction

Laser powder bed fusion (LPBF) is a three-dimensional printing (3D printing) additive manufacturing (AM) method for fabricating metallic components of complex geometry layer-by-layer[1,2]. In recent years, many applications of LPBF components have emerged (e.g. in spaceflight engineering) because it provides great design freedom, part simplification and low cost for small manufacturing runs[3]. However, the entrainment of pores/defects in the LPBF process impairs the fatigue life of final products[4], hindering its application in high structural integrity sectors, such as

aviation[5]. For this reason, understanding the physical mechanisms of pore defect formation is essential if we are to have largely pore-free additive manufacturing of LPBF products.

Many LPBF process parameters are important in terms of the relative density of LPBF parts[6], and their complex interdependence make it difficult to assess their relative importance. Among these, the effect of hatch spacing (h), laser power (P), scanning velocity (v), and layer depth (d) on relative density have been studied in two[7], three[8,9] and four[10] process parameter evaluations across many materials and applications. To simplify their consideration, the concept of the volume energy density (E) of the laser is introduced because it captures many aspects of the thermal history of LPBF products in a single parameter[11]. E represents the energy absorbed from the laser per unit volume[12] of the powder bed under ideal conditions, assuming the laser energy is completely absorbed by the powder. Hence, the relationship between E and P, v, h, d can be expressed by Equation (1) [13,14].

$$E = P/(v * h * d) \quad (1)$$

Data-driven modelling approaches are well suited to LPBF because many different process parameter sets can be explored in one high throughput printing experiment[15]. Data-driven methods have the potential to make AM more intelligent[16], continuously adapting the process parameters as complex shapes are manufactured to optimize microstructure and reduce defects and pores. In recent years, machine learning approaches have been used to capture complex process parameter-structure-property (P-S-P) relationships through various approaches including regression, Gaussian processes, naive Bayes, artificial neural networks, particle swarm algorithms, and support vector machines[17,18,19]. Compared with the time-consuming and difficult process of building physics-based models, the application of machine learning data-driven models based on physical understanding offers the prospect of faster optimization of the AM process[20].

Liu et al.[21] captured the effects of laser power and scanning velocity on relative density using a Gaussian process regression (GPR) surrogate model and obtained a maximum relative density (> 99 %) in subsequently processed parts. Shevchik et al.[22] adopted a deep convolutional neural network to classify three degrees of porosity in samples manufactured by powder-bed fusion, with classification accuracy ranging from 78 % to 91 %. Liu et al.[23] proposed a methodology combining experiments, numerical and analytical calculations to predict the porosity in terms of lack-of-fusion pores and keyhole pores for LPBF fabricated samples in relation to the characteristic dimensions of the molten pool.

Scanning electron microscopy (SEM) and optical microscopy have often been used to study pores arising from lack-of-fusion post mortem[13,24]. In-situ high frame rate synchrotron X-ray imaging has been used to study the formation and evolution of keyhole pores and lack-of-fusion during LPBF[5,25–29]. Cunningham et al.[5] used ultrahigh-speed x-ray imaging to quantify the phenomenon of vapor depressions (also known as keyholes) during laser melting in additive manufacturing. Zhao et al.[26] found that the voids generated deep inside the materials were pinned by the advancing solidification front and further revealed the detailed formation process of keyhole pores. These are caused by a critical instability at the keyhole tip which generates acoustic waves driving the pores near the keyhole tip to move away from the keyhole bottom and before being trapped by the solidification front[27]. Leung et al.[28] revealed that the pore and keyhole formation mechanisms are driven by a combination of high temperatures and high metal vapor concentrations in the keyhole with irregular pores formed via keyhole collapse and pore coalescence.

The P-v process diagram enables the exploration of process space in LPBF to simply and conveniently identify high-density conditions[30,31]. As the temperature of the molten pool (or the laser energy density) increases, there are 3 melting modes; namely a conduction mode (where heat is transferred primarily by conduction), a transition mode[32] and a keyhole mode (where convection is the dominant heat transfer mode). Lack-of-fusion pores usually occur in conduction mode while keyhole porosity in the unstable keyhole mode[31].

Data-driven methods have been used to quantify the relationship between process parameters, and LPBF characteristics by classification[22,33–35] or regression [21,36–39]. Although, machine leaning assisted /data driven find the relationship between relative density and process parameters, the lack of interpret-ability and broad applicability for these models inhibits their application in 3D printing of various metal materials. Therefore, it is very necessary and urgent to establish an interpretable universal relative density equation applicable to multiple metals to escape extensive duplication and inefficient development. In this respect, the interactions between the 4 key process parameters (P, v, h, d) and porosity (or relative density) represent a high-dimensional coordinate

system, which is difficult to visualize and intuitively understand. Nevertheless, such a relation describing their impact on porosity is needed to safely and robustly apply AM processes to the aviation industry and other critical high structural integrity sectors.

This study seeks to fill that gap, both in terms of an empirical relation, but also linking this to physics-based interpretation of the low and high laser energy density regimes. To that end a data-driven method has been employed based on a high throughput global design of experiments study to explore the extent to which various process parameters affect the relative density. This has been complemented by a data-physics fusion driven (DPFD) approach constructed to investigate the physical mechanisms through which the laser volume energy density impacts the relative density. Finally, the DPFD model are shown to be relevant to predicting relative density as a function of laser process conditions across a range of different materials and types of LPBF equipment.

2 Materials and Methods

This work fully considered the advantages and disadvantages of present researches as shown in Fig. 1. How to obtain a stable and reliable fully dense LPBF products is still a big challenge. Therefore, a data-physics fusion driven approach was proposed for establishing a universal relative density equation across various of materials which could be helpful to explore the intrinsic mechanism of relative density. The main construction procedures of a universal relative density equation are shown in Fig. 1 and the more details could be found in the following Section 2.2 - Section2.5.

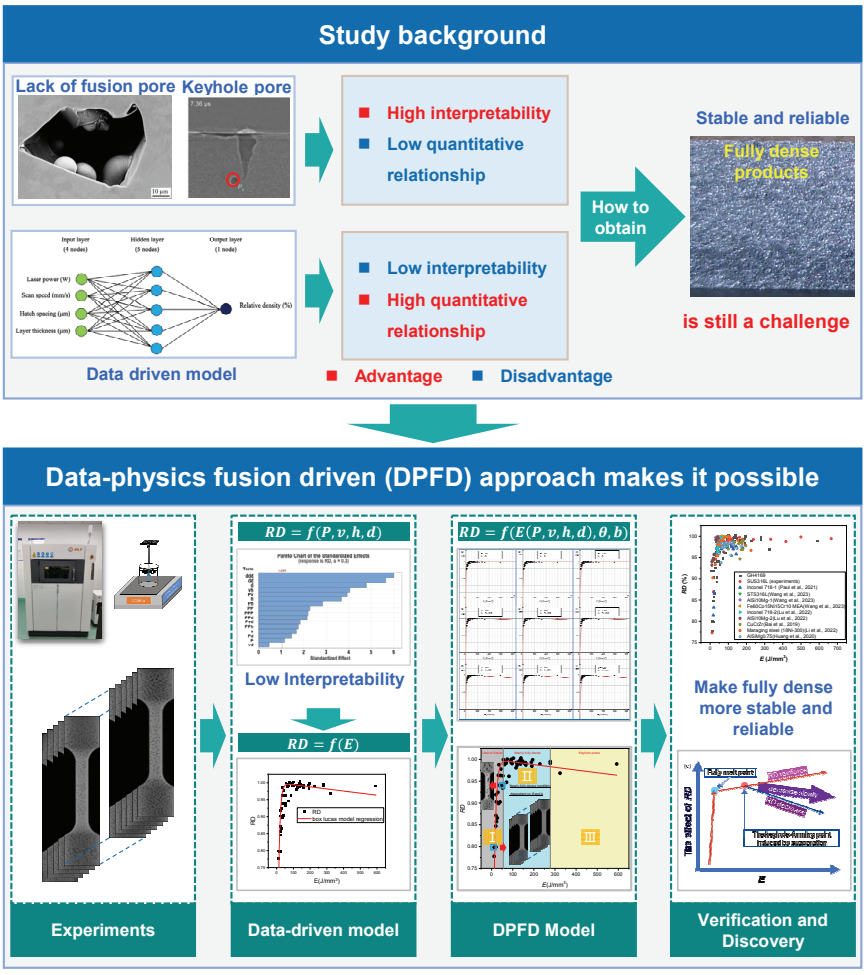

Fig. 1 The main idea diagram of this work

2. 1 Sample manufacturing

Gas-atomized GH4169 nickel superalloy powder was purchased from BLT Corporation having dimensions in the range 15 – 45 μm (particle size distribution D10 = 17 μm, D50 = 28 μm, D90 = 44 μm) and chemical composition reference standard: GB/T25829, as summarised in Table 1. The 30 mm long and 1.52 by 2.50mm gauge cross-section dog-bone samples were

manufactured by the LPBF machine (BLT-S210, Xi'an, China) under a 99.99 wt.% argon atmosphere (see Fig. 2). The LPBF machine was equipped with an advanced single-mode YAG fiber laser with a focused beam spot size of 100 μm and an infrared light laser wavelength of 1060~1080 nm easily absorbed by GH4169 powder, with a maximum laser power of 500 W. Prior to LPBF, the powder had been preheated for 4 hours at 120 ℃ to ensure flowability, and the stainless steel 304 substrate had been pretreated by sandblasting. A global, stepwise, as well as a centrally dense, orthogonal design of experiments strategy was adopted to cover the entire energy range. The process parameters (P, v, h, d) were designated into two orthogonal tables (Table $L_{49}(7)^4$ and $L_{16}(4)^3$) as shown in Table 2 and the 3D models of the samples were sliced and processed by Materialise Magics 24.0 software (Materialise, Belgium). Other parameters were selected on the basis of experience (scanning strategy: chessboard; rotation angle: 67°; shielding argon flow speed: 1.2 m/s).

Table 1 Superalloy GH4169 chemical composition (wt.%)

Value	Cr	Ni	Mo	Al	Ti	Nb	Cu	B	Co	C	Si	S	P	Mg	Mn
Min.	17.00	50.00	2.80	0.20	0.65	4.75	/	/	/	/	/	/	/	/	/
Max.	21.00	55.00	3.30	0.80	1.15	5.50	0.30	0.006	1.00	0.08	0.35	0.015	0.015	0.01	0.35
Actual value	18.98	54.66	3.15	0.48	0.98	5.00	0.034	<0.005	0.12	0.024	0.070	<0.0020	<0.01	<0.01	0.027

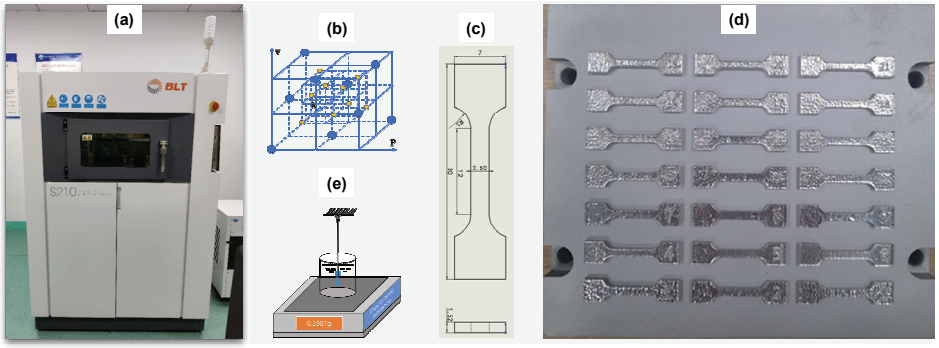

Fig. 2 LPBF samples manufacturing and relative density test: (a) LPBF equipment; (b) design of experiments; (c) engineering drawing; (d) LPBF samples; (e) illustration of relative density test

Table 2 The first (upper half) and second (lower half) orthogonal tables

o.	P (W)	v (mm/s)	h (μm)	d (μm)
Group1				
1	260	700	90	20
2	290	900	100	20
3	320	1100	110	20
4	350	1300	120	20
Group2				
1	100	300	60	20
2	150	600	75	30
3	200	900	90	40
4	250	1200	105	50
5	300	1500	120	60
6	350	1800	135	70
7	400	2100	150	80

2. 2 Relative density measurement

Relative densities were measured through an electronic balance (ATY124, SHIMADZU Corporation, Japan) with an accuracy of 0.0001 g by the Archimedes method, as show in Fig. 2. The dry and clean samples were put into the deionized water for the relative density test ensuring no air bubbles were attached to their surfaces.

2.3 Computerized tomography detection for lack-of-fusion pores

The positions and shapes of pores regions were identified by the industrial computed tomography (CT) machine with a spatial resolution of 20 μm and a slice spacing of 20 μm along the building direction. Two samples with low laser energy density 12.35 J/mm^3 (Process No. 42) and 49.38 J/mm^3 (Process No. 29) were tested.

2. 4 Data-driven model

Four key process parameters (P, v, h, d) representing the thermal history, were selected to construct the multivariate model for correlating against relative density using Minitab 19. Although 1st-order and 2nd-order models were constructed, their predictive ability was poor (R^2_{pre} < 80 %). Hence, a 3rd-order multivariate model was constructed by the stepwise regression method and the model optimized by tuning ***Alpha* to add** and ***Alpha* to remove** values to select and delete the items of the model as shown in Table 3, and the model

evaluation indices are shown in Equation ((2) – (6)). If the *P*-value corresponding to the *F*-statistic for any variable is greater than the value specified in ***Alpha* to remove** (Equation (7)), then Minitab removes the variable with the largest *P*-value from the model, calculates the regression equation, displays the results, and initiates the next step; If the *P*-value is smaller than ***Alpha* to add** (Equation (8)), Minitab adds the variable with the smallest *P*-value to the model, calculates the regression equation, displays the results, then goes to a new step. Stepwise procedure ends when *P*-values of all variables not in the model are greater than the specified ***Alpha* to add** value and when *P*-values of all variables in the model are less than or equal to the specified ***Alpha* to remove** value. The predictive model of relative density reached a high level of predictive ability when both the two ***Alpha*** values were set to 0.18. Finally, a 3rd-order good stepwise regression model correlating *P*, *v*, *h*, *d* to relative density was established.

Here S is the root mean square error and MSE ($MS\ Error$) is the mean square error:

$$S = \sqrt{MSE} = \sqrt{\frac{1}{n}\sum_{i=1}^{n}(y_i - \hat{y}_i)^2} \tag{2}$$

where n is the number samples; y_i is the i^{th} observation; $\hat{y}$ is the i^{th} fitting response. R^2 is also known as the coefficient of determination;

$$R^2 = 1 - SS\ Error/SS\ Total = 1 - \sum(y_i - \hat{y})^2 / \sum(y_i - \overline{y})^2 \tag{3}$$

where SS is the sum of the squared distances and $\overline{y}$ is the average response. $R^2{}_{adj}$ represents the adjusted R^2 as shown in Equation (4)

$$R^2{}_{adj} = 1 - MS\ Error/MS\ Total = 1 - [\sum(y_i - \hat{y})^2 / \sum(y_i - \overline{y})^2][(n-1)/(n-p-1)] \tag{4}$$

where MS is mean squares; n is the number of observations; p is the number of items in the model. $R^2{}_{pre}$ represents the predicted R^2.

$$R^2{}_{pre} = 1 - PRESS/SS\ Total = 1 - \sum_{1}[e_i/(1-h_i)]^2 \Big/ \sum_{1}(y_i - \overline{y})^2 \tag{5}$$

where e_i is the i^{th} residual error; h_i is the i^{th} diagonal element of $\mathbf{X(X'X)^{-1}X'}$. $PRESS$ is also used to evaluate the predictive ability of the model:

$$PRESS = \sum_{1}^{n}[e_i/(1-h_i)]^2 \tag{6}$$

Variables to remove: An *F*-statistic and *P*-value are calculated for each variable in the model. If the model contains j variables, then F for any variable, X_r, is this formula:

$$F = [SSE_{(j-X_r)} - SSE_j]/DF_{X_r}/MSE_j \tag{7}$$

where $SSE_{(j-X_r)}$ is the $SS\ Error$ for the model that does not contain X_r; SSE_j is $SS\ Error$ for the model that contains X_r; MSE_j is $MS\ Error$ for the model that contains X_r.

Variables to add: If Minitab cannot remove a variable, the procedure attempts to add a variable. Minitab calculates an *F*-statistic and *P*-value for each variable that is not in the model. If the model contains j variables, then F for any variable, X_a, is this formula:

$$F = [SSE_j - SSE_{(j+X_a)}]/DF_{X_a}/MSE_(\tag{8}$$

where SSE_j is $SS\ Error$ before X_a is added to the model; $SSE_{(j+X_a)}$ is $SS\ Error$ after X_a is added to the model; DF_{X_a} is degrees of freedom for variable X_a; $MSE_{(j+X_a)}$ is $MS\ Error$ after X_a is added to the model.

Table 3 Evaluation indexes of relative density prediction model

Prediction model	S	R^2	$R^2{}_{adj}$	$R^2{}_{pre}$	*Alpha to add*	*Alpha to remove*
Relative density	0.016	94.7 %	92.7 %	86.8%	0.3	0.3

2. 5 Data-physics fusion driven model

The upper data driven model of stepwise regression can provide a relatively high precision in predicting the relative density. However, it is poor interpretability which lead to it cannot find the general rules of dense suitable for various of metal materials in LPBF. Subsequently, considering the heat history, the relative density equation including the relationship between *E* and *RD* was developed via Box-Lucas model fitting which could decrease the dimensions of input variables and also contain useful heat information *E*. Although the Box-Lucas model of *RD* can promote understanding of the intrinsic mechanisms of *RD* to a certain extent, its goodness of fit R^2 is poor and not as good as the stepwise model. To confirm that the Box-Lucas model indeed reflects general rules of *RD*, the predictive results provided by stepwise model were used to verify whether the Box-Lucas model is reasonable. The detail processes are as follows.

10000 groups of artificial process parameter data were generated with parameters uniformly distributed across the ranges of *P* (50-500 W), *v* (300-3000 mm/s), *h* (60-150 μm) and *d* (20-80 μm) and the energy density for each calculated using Equation (1). The simulated data

for *RD* were predicted using a 3rd-order stepwise regression model to form *E-RD* data pairs to test the capability of the Box-Lucas model[40]. The basic trend of the predicted results is consistent with the trend reflected by the Box-Lucas model, which proved that the Box-Lucas model is helpful in exploring the intrinsic mechanism of *RD*.

However, since it simply considered *E* rather than the four process parameters, it can not explain why a wide range of *RD* is observed for the same *E* which is the main reason of its low R^2. one *E* value can be composed of countless combinations of process parameters. These process parameters can induce various of different melt pool temperatures and then lead to different shapes of weld beads. Therefore, it is reasonable to speculate that the Box-Lucas model does not include some important influencing factors. For this reason, a DPFD model was constructed by introducing contact angle (θ)[41] and boiling factor (b) into the Box-Lucas model to cover all the data in the *E-RD* coordinate system. The data-physics fusion driven model was inspired by the Morse potential energy function (Equation (12))[42], but is more complicated due to its dynamic changes.

3 Results and discussion

3.1 Relative density test results

Table S1 shows the process parameters and relative density measurement data across the global LPBF process parameter window. The first and second groups of orthogonal experimental results were recorded in No. 1 – No. 16 and No. 17 – No. 65, respectively (see Table S1). Bulk samples were successfully manufactured using all the process parameters selected except for trial No. 49 in group 2 where the powder did not become molten under such a low energy density (6.17 J/mm^3). The sample with a nominally tested relative density of 100 % was obtained from trial No. 34 in the second group (P = 250 W; v = 600 mm/s; h = 75 μm; d = 40 μm). All the relative densities of LPBF samples in the first group of orthogonal experiments are higher than 98 %, however there is a wide distribution of relative densities from about 52 % to 100 % in the second group.

The scatter points of process parameters and relative density is shown in Fig. 3. It is very difficult to obtain fully dense products, because pores could be occurred in each level of process parameter such as low *P*, middle *P* and high *P* (Fig. 3 (a)). Fig. 3 (b) is drawn based on all the tested data recorded in Table S1, without considering the other two parameters when drawing the P-v color map. Controlling *RD* only through two parameters P-v is also adventurous, as changes in the other two parameters will lead to variations in the optimal process window (Fig. 3 (b)).

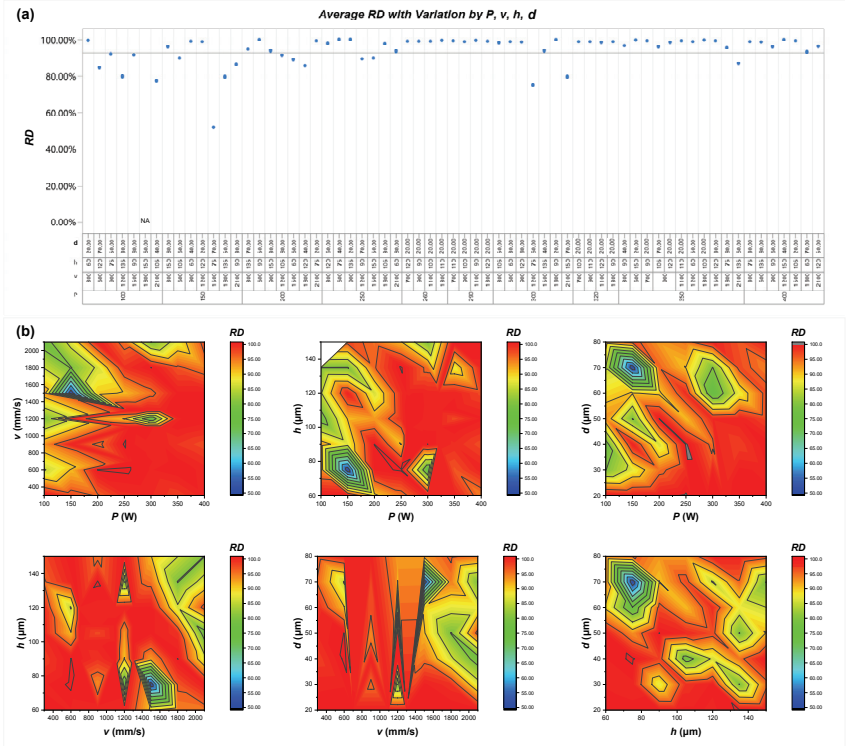

Fig. 3 The complex nature of the impact of the process parameters on relative density (*RD*): (a) the *RD* as a function of the process parameters; (b) the color map of *RD* and each two parameters pair and note that other two hidden parameters are not immutable

3.2 CT detection results

From Fig. 4, Two types of pores with different morphologies are easily found in low *E* samples through CT detection. Larger scale pores with more irregular

morphologies and fewer in number in Fig. 4 (a) are lack-of-fusion pores due to lower laser energy (12.35 J/mm^3) input for LPBF forming. In contrast, the smaller scale pores with relatively dispersed and more uniform distribution as well as a large number of dots' morphologies in Fig. 4 (b) are lack-of-fusion pores because of higher laser energy (49.38 J/mm^3) input during LPBF forming. Especially, the larger lack-of-fusion pores exhibit an obvious interlayer penetration phenomenon. These apparent differences prompt us to DPFD model to uncover their underlying physical mechanisms later.

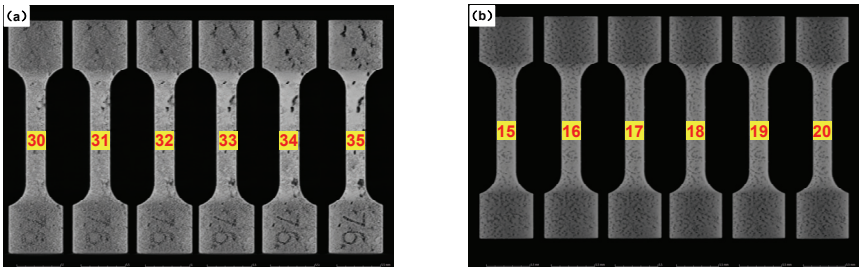

Fig. 4 Lack-of-fusion pores in CT detection as well as the number of slice layers yellow labelled on the samples; (a) lack-of-fusion pores with E = 12.35 J/mm^3; (b) lack-of-fusion pores with E = 49.38 J/mm^3

3.3 Data-driven model and predicted results

Considering the 4 key process parameters (*P*, *v*, *h*, *d*), a multivariate regression model was employed to explore the complex dependency of relative density (or porosity) on these parameters summarised in Fig. 3. A 3rd-order stepwise regression method was applied. Firstly, all the 3rd-order relations between laser power, scanning velocity, hatch spacing, power thickness, and their interaction function were introduced to construct a regression model of relative density. Furthermore, to obtain the most appropriate fitting, the model was optimized by tuning ***Alpha* to add** and ***Alpha* to remove** values for removing the insignificant constructing items of the model and remaining the significant items (as shown in Table 3 and Table 4). The final best-fit regression model is summarised by Equation (9) with the coefficients defined to a precision of 10 decimals in Table 4.

Table 4 Coefficient statistical test and variance analysis of relative density model

Term	Coef	SE Coef	T-value	P -value	VIF	Source	DF	Adj SS	Adj MS	F -value	P -value
Constant	0.8500128767	0.0866809064	9.81	0.000		Regression	16	0.195322	0.012208	47.25	0. 000
P	0.0011569549	0.0009975705	1.16	0.253	1705.53	P	1	0.000348	0.000348	1.35	0. 253
v	-0.0000644759	0.0000382600	-1.69	0.099	101.62	v	1	0.000734	0.000734	2.84	0. 099
h	-0.0025762963	0.0007002903	-3.68	0.001	77.67	h	1	0.003497	0.003497	13.53	0. 001
d	0.0168158479	0.0035112808	4.79	0.000	1220.33	d	1	0.005926	0.005926	22.94	0. 000
P*P	-0.0000075477	0.0000033105	-2.28	0.028	4917.23	P*P	1	0.001343	0.001343	5.20	0. 028
d*d	-0.0003944023	0.0000699407	-5.64	0.000	4302.80	d*d	1	0.008216	0.008216	31.80	0. 000
P*v	0.0000005560	0.0000001413	3.93	0.000	155.33	P*v	1	0.003999	0.003999	15.48	0. 000
P*h	0.0000165045	0.0000058103	2.84	0.007	1015.77	P*h	1	0.002085	0.002085	8.07	0. 007
P*d	-0.0000130571	0.0000088672	-1.47	0.148	777.49	P*d	1	0.000560	0.000560	2.17	0. 148
v*h	-0.0000007579	0.0000001869	-4.05	0.000	35.75	v*h	1	0.004247	0.004247	16.44	0. 000
v*d	0.0000004144	0.0000008799	0.47	0.640	257.92	v*d	1	0.000057	0.000057	0.22	0. 640
P*P*P	0.0000000081	0.0000000037	2.20	0.033	1112.32	P*P*P	1	0.001250	0.001250	4.84	0. 033
d*d*d	0.0000028445	0.0000004740	6.00	0.000	1278.05	d*d*d	1	0.009305	0.009305	36.02	0. 000
P*P*h	-0.0000000197	0.0000000111	-1.77	0.084	731.58	P*P*h	1	0.000812	0.000812	3.14	0. 084
P*P*d	0.0000000410	0.0000000190	2.16	0.036	540.39	P*P*d	1	0.001211	0.001211	4.69	0. 036
P*v*d	-0.0000000059	0.0000000032	-1.85	0.071	354.05	P*v*d	1	0.000886	0.000886	3.43	0. 071
						Error	42	0.010851	0.000258		
						Total	58	0.206173			

$$RD = 0.85 + 0.001157\,P - 0.000064\,v - 0.002576\,h + 0.01682\,d - 0.000008\,P*P - 0.000394\,d*d + 0.000001\,P*v + 0.000017\,P*h - 0.000013\,P*d - 0.000001\,v*h + 0.000000\,v*d + 0.000000\,P*P*P + 0.000003\,d*d*d - 0.000000\,P*P*h + 0.000000\,P*P*d - 0.000000\,P*v*d \quad (9)$$

To better evaluate and reflect the validity of the RD-predicted model, S, R^2_{adj}, R^2_{adj}, and R^2_{pre} were calculated, and their values are shown in Table 3. The indexes ***Alpha* to add** and ***Alpha* to remove** in Table 3 were applied to select and delete items of the model for model optimization. The ***Alpha*** values were typed in to determine whether items can be added into or removed from the model. From Table 3, S is slightly lower than 0.02 and the coefficient of determination R^2 is 94.7 %, illustrating the good fitting ability of the model. The R^2_{pre} value was adjusted to the maximum value by tuning the ***Alpha*** values to delete such insignificant items and retain the significant items to gain the optimal generalization capability of the model. When the two ***Alpha*** values were set as 0.3, the model reached optimal. Meanwhile, the stepwise procedure ends when the P-values of all items not in the model were greater than ***Alpha* to remove** = 0.3 and the P-values of all items except $v*d$ in the model were less than or equal to ***Alpha* to add** = 0.3 (Table 3 and Table 4).

From Table 4 and Fig. 5 (a), it is evident that the strongest to weakest influence on relative density of the process parameters is the hatch spacing followed by the laser power, scanning velocity, and layer depth according to the P-values or the Pareto effects. In the normal probability graph (Fig. 5 (b)), these points are almost arranged in a line, indicating that there is no evidence to prove that the distribution of residuals is non-normal. From Table 3, the root mean square error of relative density is less than 0.02, which illustrates the model has been optimized well under a global condition.

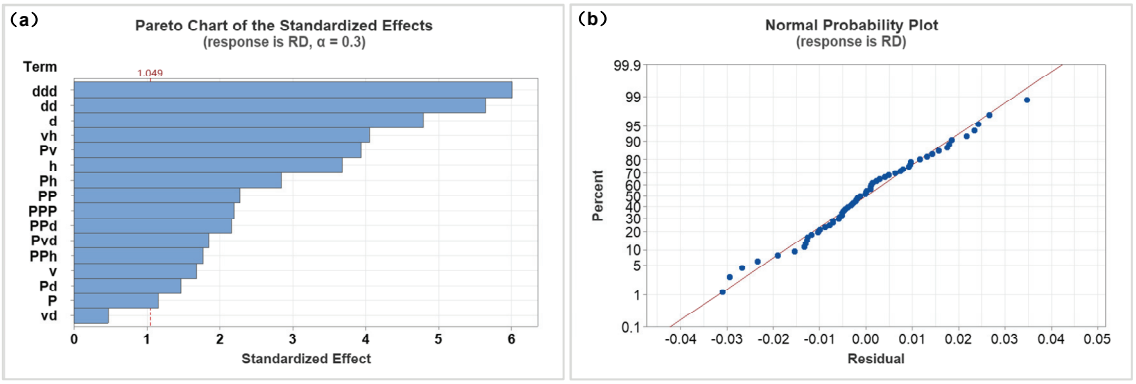

Fig. 5 Relative density model evaluations: (a) Pareto chart for the influence degree of terms on relative density; (b) normal probability plot

3.4 Data-physics fusion driven (DPFD) model

Although the stepwise regression model suggests the relative importance of key process parameters on relative density, it does not contain any materials' characteristics or environmental conditions. To do this we employ a DPFD model constructed as follows: firstly, a relationship between E and RD was established after removing the abnormal data, and the mathematical model of E and RD was constructed from experimental data. Subsequently, the DPFD model was developed to make up the shortcomings of this simple model. Finally, the DPFD model was validated using multiple sources, including simulated data, experimental data, and reference reported data [39,43–48].

As shown in Fig. 6 (a), several datapoints were abnormal according to the residual error analysis. Both the stepwise regression model and the Box -Lucas model were constructed after deleting the same abnormal data recognized by the residual error diagnosis, as shown in Fig. 6 (a) inset. To quantify the impact of the energy density of the laser on relative density, the Box-Lucas model was introduced to regress for the energy density of the laser (E) and relative density (RD) as shown in Fig. 6 (b), and the original Box-Lucas model was expressed using the following Equation (10)[40]:

$$\eta = \theta_1/(\theta_1 - \theta_2)\left[exp\ (-\theta_2\,\xi_1) - exp\ (-\theta_1\,\xi_1)\right] \quad (10)$$

where η is the yield of intermediate product B in a

consecutive chemical reaction (A→B→C); θ_1 and θ_2 are constants measuring the specific rates of the first and second decompositions, respectively; ξ_1 is elapsed time. The *RD* model was optimized by the Levenberg-Marquardt iterative algorithm until convergence (Equation (11) and Table 5):

$$RD = a_1/(a_1 - a_2)\left[exp\left(-a_2E\right) - exp\left(-a_1E\right)\right] \quad (11)$$

Moreover, the results of the regression indicate that the fitting ability of the model is not as good as the stepwise model for *RD* (R^2 = 71 % compared to 94 % for the stepwise model, as shown in Table 3 and Table 5). It should be noted that the Box-Lucas model curves cannot explain all the relative density data because one *E* can correspond to a wide range of *RD* values (see Fig. 6 (b) and Fig. 6 (c)). Therefore, it is necessary to develop less naive models to explore the effect of processing on *RD*.

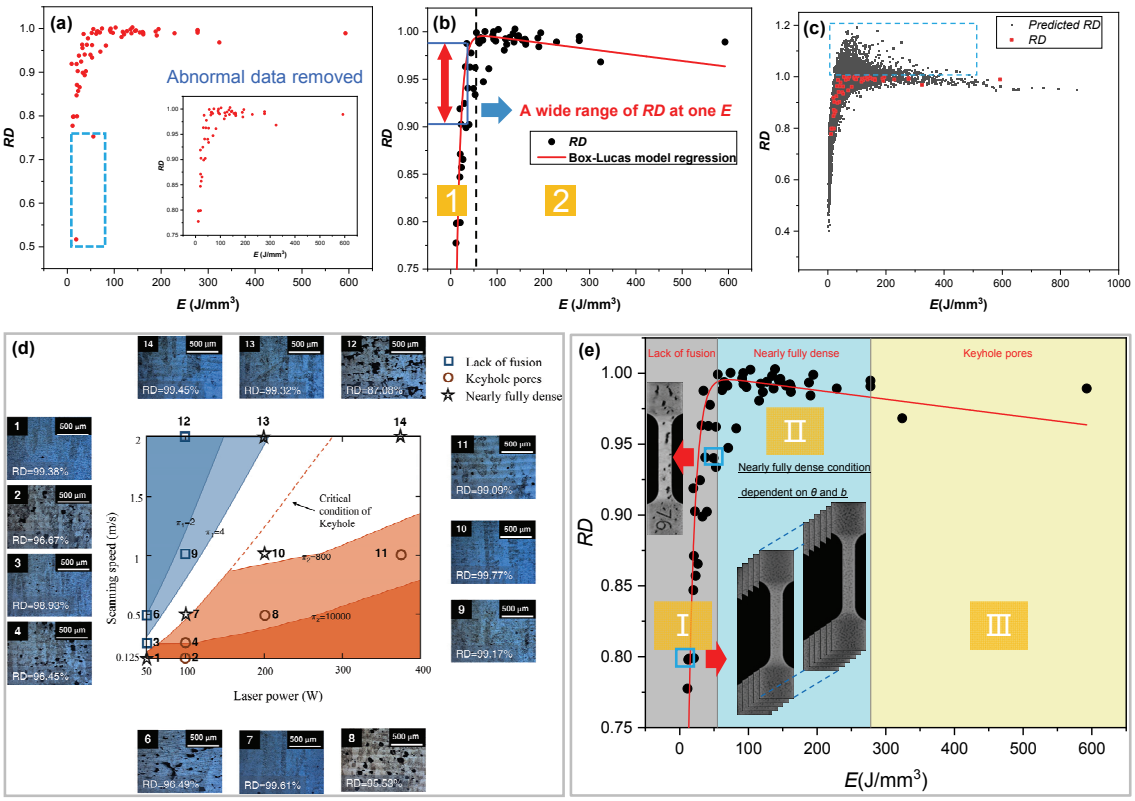

Fig. 6 The relationship between the energy density, E, of the laser and relative density, RD: (a) the scatter point diagram for the experimentally measured relative density and energy density and the abnormal points removed inset; (b) Box-Lucas regression model; (c) 10000 datapoints simulated using Equation (9) (no upper boundary of predicted *RD* set); (d) P-v processing window predicting porosity defects of Ti-6Al-4V agrees with the cube sample results [23] (it means three regimes in the pore state in the *P-v* coordinate system); (e) three regimes in energy density interval

Table 5 The regression results of the relationship of E and RD constructed by the Box-Lucas model.

Box - Lucas model	a_1	a_2	R^2	R^2_{adj}
Relative density	1.05E-1±3.8E-3	6.3E-5±3.2E-5	71.2 %	70.7 %

To capture more of the physics, a physics-based approach is proposed based on two material characteristics, namely the contact angle (θ) and the boiling factor (b)[31], as illustrated in Fig. 7 (a). This reflects the fact that these are believed to determine the relationship between *E* and *RD* in the low *E* and high *E* regions, respectively. The model originates from the Morse potential energy function, as shown in Equation (12)[42]. Then the universal relative density equation is established by introducing the factors θ and b, as shown in Equation (13).

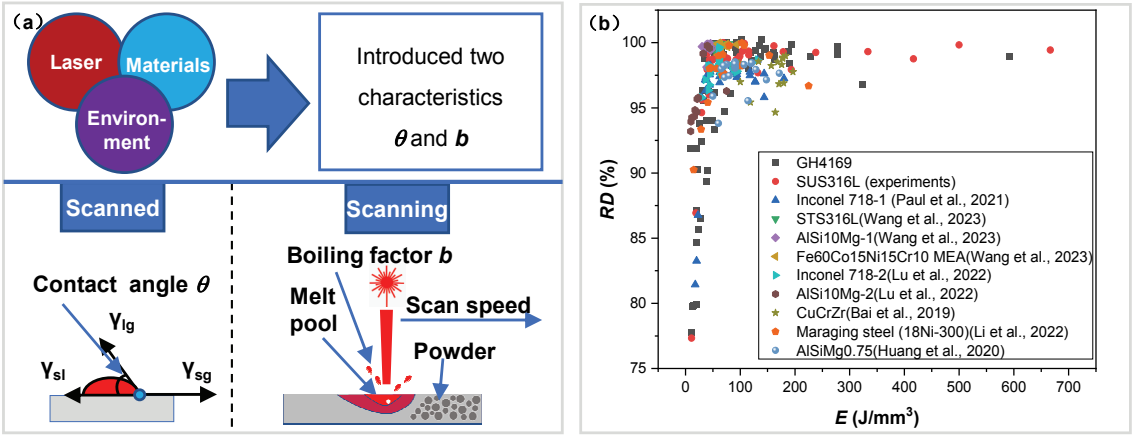

Fig. 7 The whole consideration of laser, material and environment, and multi-materials validation: (a) the illustration of introducing two characteristics *θ* and *b*; (b) multi-materials validation[39,43–48]

$$E(r) = Dexp[-2\beta(r-r_0)] - 2Dexp[-\beta(r-r_0)] \tag{12}$$

$$RD = \left(\left[(\cos\ \theta+1)/C+b\right]/\left[(\cos\ \theta+1)/C-b\right]\right)\cdot\{exp(-b\cdot E) - exp\left[-(\cos\ \theta+1)/C\cdot E\right]\} \tag{13}$$

where θ is the contact angle; C is a constant and when C = 10, the model is the special case suitable for GH4169 alloy; b is the boiling factor which measures the contribution of metallic vapor to the formation of pores and is also relative to environment; and E is the volume energy density of the laser. The model (we termed it as the RD dynamic sickle model) is shown graphically in Fig. 8 and the general expressions are shown in Equation (14) and Equation (15).

$$RD = \{[T(\theta)+b]/[T(\theta)-b]\}\cdot\{exp\,(-b\cdot E) - exp\ \ [-T(\theta)\cdot E]\} \quad \text{where } T(\theta) = (cos\,\theta+1)/C \tag{14}$$

$$RD = RD_0\cdot\{exp\,(-b\cdot E) - exp\ \ [-T(\theta)\cdot E]\}$$
$$\text{where } RD_0 = [T(\theta)+b]/[T(\theta)-b] = \left[(\cos\ \theta+1)/C+b\right]/\left[(\cos\ \theta+1)/C-b\right] \tag{15}$$

which becomes

wherein $T(\theta)$ is the item related to wettability (mainly dependent on the materials and the temperature of the molten pool). The initial value of RD_0 is near to 1 and is related both the wetting characteristics (θ) but also the boiling factor (b).

The model is consistent with the essential physics. In the low E region, as the wettability increases (or the contact angle (θ) decreases), the relative density increases rapidly to 1, as illustrated in Fig. 8 (a) – Fig. 8 (c). In the high E region, the relative density is dependent mainly on the boiling factor (b) decreasing slowly with increasing b, as shown in Fig. 8 (a), Fig. 8 (d), and Fig. 8 (g). Critically, the model is validated by different kinds of material data, as shown in Fig. 7 (b), including our experimental data and previously reported data [39,43–48], generated by different materials, environments, and process parameters (heat history).

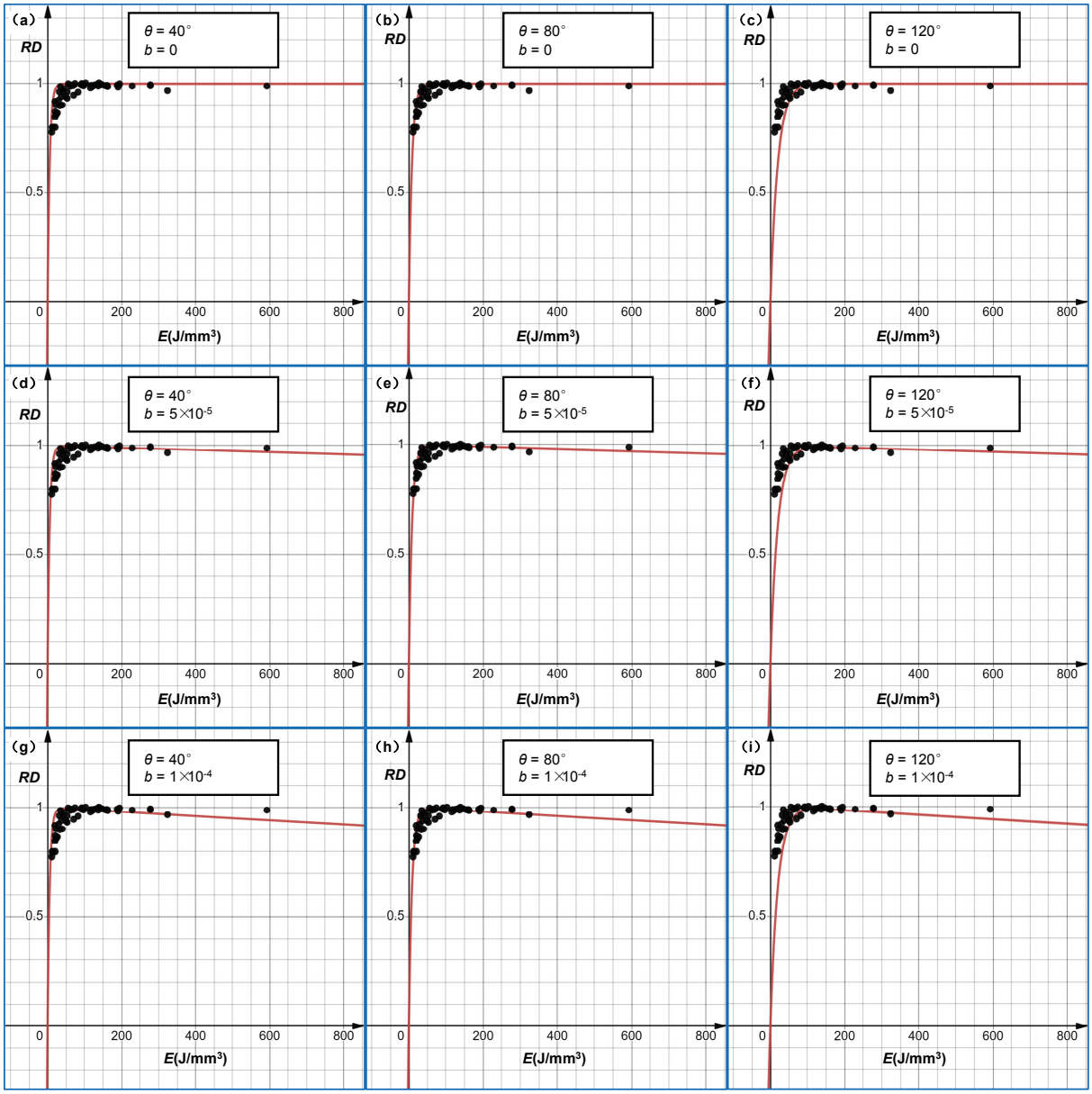

Fig. 8 The RD relationship model constructed with the factors *E*, *θ*, and *b*: (a) – (c) *b* =0 and *θ* = 40°, 80°, 120°, respectively; (d) – (f) *b* = 5 × 10^{-5} and *θ* = 40°, 80°, 120°, respectively; (g) – (h) *b* = 1 × 10^{-4} and *θ* = 40°, 80°, 120°, respectively

4. Discussion

Pore defects are the main reason of density loss[49]. At present, research on machine learning assisted LPBF parameter optimization mainly focuses on limited processing parameters (such as laser power and scanning speed). It lacks comprehensive consideration of factors that affect the process, such as thermal history[50]. Our research provides a comprehensive perspective on how thermal history affects relative density.

Our results summarised in Fig. 6 (a,b) show, in common with previous work[46,48,51], that there are two sub-optimal regimes in the *E vs RD* parameter space; the lower energy density and the high energy density regime. This is consistent with there being two competing effects on the relative density. Here two factors, namely the contact angle (θ) and the boiling factor (b), were employed to simulate the *E vs RD* curve. In the low *E* regime, porosity is mainly dependent on the contact angle (θ)[52]. In the high *E* regime, since porosity commonly occurs after the molten pool begins to evaporate[27], porosity is mainly affected by the boiling factor.

The results are consistent with these physical effects. In the extremely low *E* region, the energy from the laser cannot melt the powder and the bulk sample cannot form, which was validated by the experimental result of No. 49

(*RD* = NA). As *E* continues to increase, the powder particles begin to partially melt[53], however the relative density is only marginally in excess of that for closely packed spheres (74%) with the *RD* of No. 32 being 77 % and No. 48 being 75 %, respectively. At this stage, the most influential factor has transformed from the wettability of the powder particles to the wettability of the weld bead. In the relatively low *E* region, the porosity existing at the interface of weld beads has been observed to be lack-of-fusion pores[23] (Fig. 6 (e)). As the *E* increases further, all the powder can be melted fully in weld bead, and the wettability improves further[54–56] and the *RD* increases, mainly dependent on the contact angle in the *E*-*RD* coordinate system, till the temperature reaches the boiling temperature of GH4169 powder.

In this *E* regime, the wettability nearly reaches its peak, but as the *E* increases further, metal vapor starts to form, and the recoil pressure causes the molten pool to form a vapor depression (keyhole). This causes the protecting gas to become entrained into the molten pool by the recoil pressure, Marangoni force, and laser pressure. The entrained gas captured by the front of the solid-liquid interface is relatively finite in the high *E* region, except that the materials are completely governed by the vapor, like laser cutting. In this global process parameter window, the maximum *E* (close to 600 J/mm^3) is already sufficiently large (Table S1) that the relative density in the high *E* region is unlikely to be lower than 95 %.

In effect the process window is divided into 3 zones in *P*–*v* space, namely the lack-of-fusion zone, the nearly fully dense zone (optimal process window), and the keyhole pore zone (Fig. 6 (d))[22,30]. The results are in accord with our experimental data (Fig. 6 (e)). In a single curve of *E*-*RD*, there is only a single broad maximum however the four laser parameters give rise to a more complex parameter space which can be captured by the four-parameter empirical regression analysis.

To further demonstrate the universality of the constructed *RD* theory, we further measured the wetting angle of the weld bead in reference[57] (Fig. 10 (a)) and calculated the corresponding laser energy density under different process parameters according to Equation (1) (assumed the hatch spacing is 100 μm and layer thickness is 30 μm), and recorded the process parameters and wetting angles (Fig. 10 (b)). After that, a two-dimensional scatter plot was drawn between the wetting angle and energy density (Fig. 10 (c)). Due to the complete negative correlation between the value of wetting angle and wetting properties, to provide a more intuitive display, we introduced 180 ° - θ to represent the size of the wetting properties of weld bead and drew a graph of the influence of wetting properties on density (Fig. 10 (d)). There is an inflection point in wettability, that is a fully melted point of bead, which divide the laser energy density interval into 2 parts, interval 1 and interval 2 (Fig. 10 (d)). Interval 1 reflects that in this energy range, insufficient energy leads to incomplete melting of the bead, resulting in a coexistence of solid and liquid phases in the melt pool. Due to the presence of solid phases, the wettability increases sharply with increasing energy density. Interval 2 reflects that after the bead is completely melted, the wettability of the melt does not sharply increase with the increase in energy density. Since wettability reflects the properties of the liquid within the melt pool, once the solid phases have completely disappeared, no factors greatly affecting the wettability can occur thereafter. The wettability relatively slowly increases as the temperature increases.

The contact angle θ (as shown in Fig. 7 (a)) can be derived from the Young's equation (Equation (16))[58]:

$$\gamma_{sg} = \gamma_{sl} + \gamma_{lg}\cos\theta \tag{16}$$

$$\theta = \arccos\frac{\gamma_{sg} - \gamma_{sl}}{\gamma_{lg}} \tag{17}$$

where γ is the surface tension between any two phase interfaces in the gas, liquid, and solid phases denoted by s, l, and g, respectively. The gas-liquid interfacial tension is temperature dependent, as shown in Equation (18)[59]:

$$\gamma_{lg} = \gamma_{lm} + A_\gamma(T - T_m) \tag{18}$$

where γ_{lm} is the gas-liquid interfacial tension at the melting point; A_γ is the surface tension gradient. γ_{lg} of GH4169 alloy decreases with temperature increases, as shown in Fig. 9. The characteristics of GH4169 are: T_m=1610 K, γ_{lm} = 1.81 N/m, A_γ = −3.7 × 10^{-4} Nm^{-1}K^{-1}, $\gamma_{lg}(T_m)$=1.81 Nm^{-1}. The solid-liquid interfacial tension can be calculated by Equation (19)[60].

$$\gamma_{sl}(T) = \beta\frac{\Delta S_m}{N_A^{1/3}V_M^{1/3}}T \tag{19}$$

where N_A is Avogadro's number, ΔS_m is the molar entropy of fusion, V_m is the molar volume of the solid, β = 0.86 for fcc and hcp and β = 0.71 for bcc, respectively. V_m can be calculated by Equation (20)[61].

$$V_m = \frac{M}{\rho_s(T)} \tag{20}$$

where M is the molar mass and ρ_s is the density of the

solid. ΔS_m satisfied Equation (21) at the melting poin [61].

$$\Delta S_m = \frac{\Delta H_{fus} \cdot M}{T_m} T \tag{21}$$

where ΔH_{fus} is melting enthalpy, here ΔH_{fus} = 227J/g. according to the above equation, $\gamma_{sl}(T_m)$ = 0.3481 Nm^{-1}. The gas-solid interfacial tension can be calculated by Equation (22)[62].

$$\gamma_{sg}(T) \approx 1.2\gamma_{lm}\left[1 - 0.229\left(\frac{T}{T_m} - 1\right) + 0.01\left(\frac{T}{T_m} - 1\right)^2\right] \tag{22}$$

Here, $\gamma_{sg}(T_m)$ =2.172 Nm^{-1}. Therefore, the following relationship is established.

$$\gamma_{sg}(T_m) > \gamma_{sl}(T_m) + \gamma_{lg}(T_m) \tag{23}$$

Therefore, there is no equilibrium state at the solid-liquid-gas three phase boundary and the melting pool will spread until solidification. This result is consistent with the literature[61] but with different materials. The contact angle increases with the increase of scanning speed and scanning spacing; The contact angle increases first, then decreases, and finally stabilizes with the increase of scanning layers[63]. These results and the DPFD model motivate us to study the evolution of contact angle with energy density.

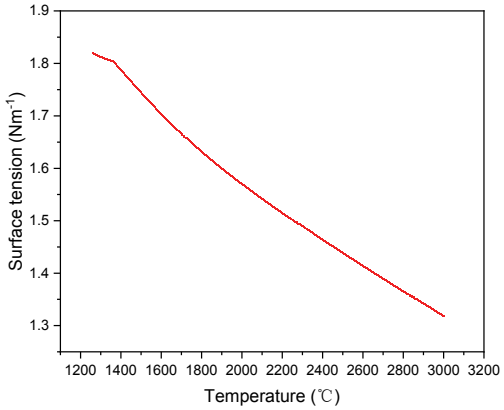

Fig. 9 Surface tensions of GH4169 change with temperatures calculated by JMatPro software

There is a physically significant characteristic temperature point not far after the fully melted point, which is the keyhole-forming point induced by evaporation[27] (Fig. 10 (e)). After this point, the wettability not only reinforces density but there is also a new effect that decreases density. As the energy increases, the evaporation effect becomes more significant, causing the tip of the vapor depression to detach and form an unstable keyhole, which is then captured by the solid-liquid interface of the melt pool during solidification[27], resulting in a relative density decrease. The final density decreases slowly due to the combined effects of these two competing factors, which were proven by our measurement data (Fig. 10 (f)) and revealed by Equation (15).

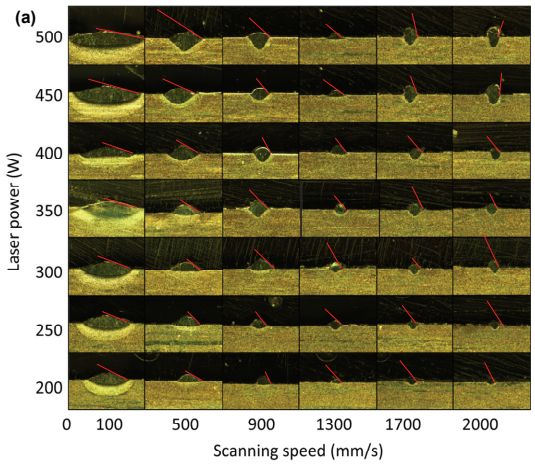

(b)

P	V				θ
500	10	33	42	40	76	110
450	15	24	50	36	69	96
400	18	29	61	52	49	50
350	16	34	45	49	63	63
300	20	40	44	60	51	65
250	22	46	52	43	53	57
200	27	29	65	47	51	63
	100	500	900	1300	1700	2000

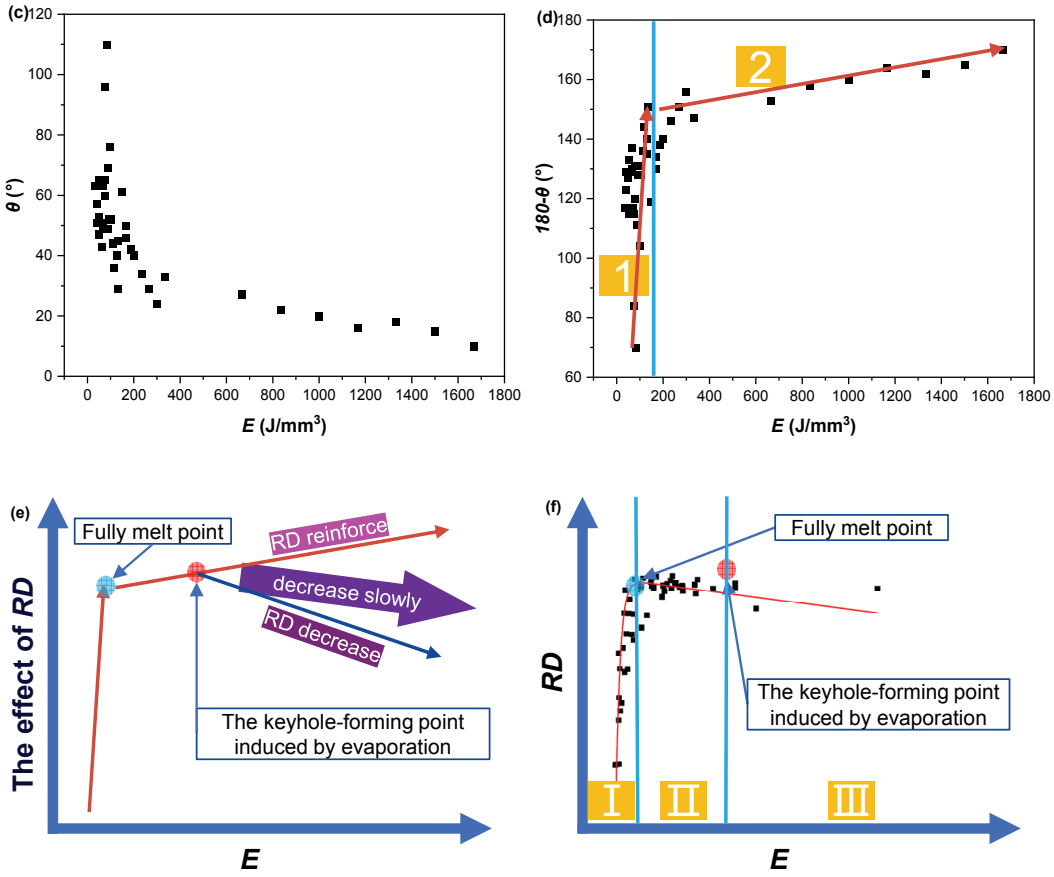

Fig. 10 The physical mechanism of relative density: (a) the reprinted figure in reference[57] and we further measured the contact angle (*θ*) of weld bead; (b) *θ* in deferent laser power (P) and scanning speed (V); (c) contact angle along with *E*; (d) 180°-*θ* along with *E*; (e) the influence of characteristic temperature points on relative density; (f) three regimes could be divided by characteristic temperature point

Fig. 11 (a) illustrates two re

gions of contact angles, region 1 and region 2, which are delineated by the melt points of cast iron, specifically the start melt point at 1140 ℃ and the fully melted point at 1220 ℃ (Fig. 11 (a) and (b)). These regions are in accordance with the results shown in Fig. 10 (c) and (d). Region 1 represents a fuzzy region (where solid and liquid phases coexist) with temperatures below the fully melted point (1220 °C), in which the contact angle sharply decreases as the heating temperature increases. Conversely, region 2 represents a fully melted region with temperatures exceeding the fully melted point (1220 °C) corresponding to the inflection point, in which the contact angle slowly decreases as the heating temperature increases. The results provide valid evidence of the fully melted point as shown in Fig. 10 (e) and (f).

The difference between Fig. 10 (c) and Fig. 11 (a) lies in the fact that the changes in contact angle are dispersed in Fig. 10 (c), but smooth in Fig. 11 (a). This difference arises from the same energy density E resulting in different energy absorptions by the powder/weld bead, furtherly generating different temperature of a weld bead in LPBF printing, insight from the following Equation (24) in the literature[1].

$$v\cdot\frac{1}{2}\pi\left(d^2+\frac{h^2}{4}\right)\cdot\frac{1}{2}\rho_{\text{material}}\cdot\left(\int C_s\mathrm{d}T+L\right)=\alpha_\lambda\cdot P \tag{24}$$

Where ρ is density; C_s is the temperature-dependent specific heat capacity of the solid; L is the latent heat of fusion; α_λ is the absorptance of the material to the laser irradiation of wavelength, λ.

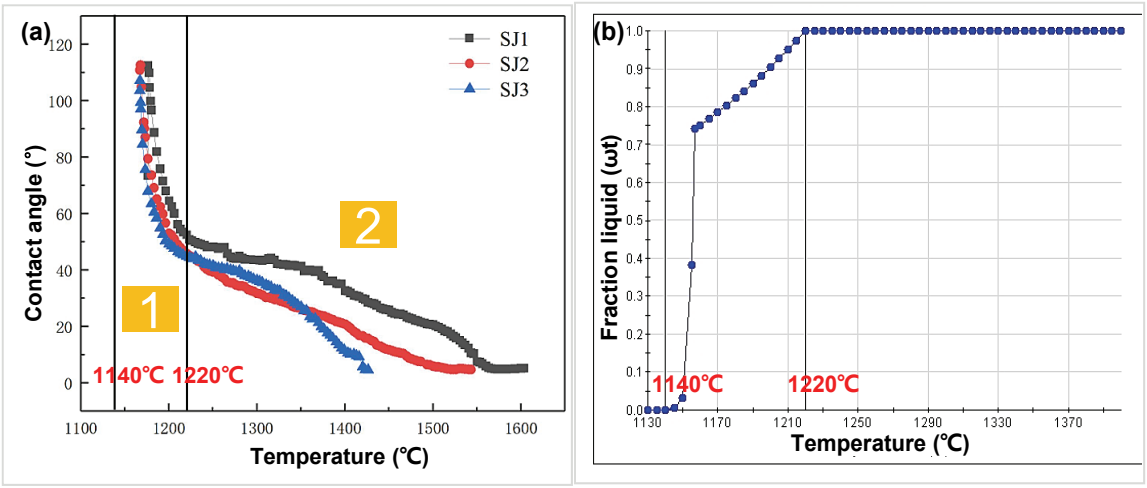

Fig. 11 The relationship between contact angles (*θ*) and heating temperature: (a) Contact angles of cast iron change with temperature, modified by reference [64]; (b) melt points of cast iron ranges from 1140 ℃ to 1220 ℃ calculated by JMatPro software

5 Conclusions

(1) A data-physics fusion driven approach is proposed to explore the origins of porosity or relative density in LPBF metal additive manufacturing.

(2) A 3rd-order empirical stepwise regression model was constructed between laser power (*P*), scanning velocity (*v*), hatch spacing (*h*), layer depth (*d*), and relative density. The results of statistical analysis suggest that the importance of the process parameters in determining relative density are in the order layer depth > hatch spacing > scanning velocity > laser power.

(3) In the global process window, 4 regimes were discussed; 1) Powder not sintered or fused (*RD* = NA), 2) Powder partially sintered or fused (*RD* < 74 %), 3) Powder completely sintered or fused (74 % < *RD* <100 %), 4) Molten pool vaporisation (95 % < *RD* <100 %). Neglecting the unmanufacturable regime, the process window could be divided into 3 regimes according to the volume energy density of the laser, corresponding to a lack-of-fusion regime (too low *E*), a highly dense region (intermediate *E*) representing the optimal process conditions, and a keyhole region (too high *E*).

(4) A DPFD model of relative density has been constructed in the *E vs RD* coordination system by introducing contact angle (*θ*), and boiling factor (*b*) which measures the contribution of metallic vapor to the formation of pores and is also relative to environment. The relative density increases rapidly as *E* increases in the low *E* regime, but it falls slowly as *E* exceeds the optimal range (process window); Meanwhile, the density rapidly increases as *θ* decreases in the low *E* regime, but it falls slowly as *b* increase when *E* exceeds the optimal process window.

(5) The DPFD model results and subsequent analysis uncover the optimal process window (intermediate *E*) boundaries are the starting point of the fully melted point and endpoint of the keyhole pores formation point. Compared with the traditional *P-v* process diagram, the model expands the design freedom of process parameters from 2 parameters (laser power, scan speed) to 4 parameters (laser power, scan speed, hatch spacing, layer thickness).

(6) A simple 2-parameter physics model explains the general trend for a variety of materials manufactured by LPBF providing a new starting point for producing fully dense products manufactured from LPBF across a range of materials.

Acknowledgments

The authors acknowledge financial support from the National Key Research and Development Program of China (grant No. 2020YFB1710100), the KGW Program (grant No. 2019XXX.XX4007Tm), the National Natural Science Foundation of China (grant No. 52275337, grant No. 51905188, grant No. 52090042), the Natural Science Foundation of Hubei Province, China (grant No. 2022CFB770). The authors would like to thank Dr. Wei Guo from Huazhong University of Science and Technology for his helpful advice on the paper.

Conflicts of interest:

The authors declare that they have no known competing financial interests or personal relationships that could have appeared to influence the work reported in this paper.

Table S1 The process parameters and relative density measurements data

Process NO.	*P*	*v*	*h*	*d*	*E*	*RD*	*porosity*
1.	260	900	90	20	160.49	99.23	0.77
2.	260	1100	100	20	118.18	99.26	0.74
3.	260	1300	110	20	90.91	99.63	0.37
4.	260	700	120	20	154.76	99.13	0.87
5.	290	900	100	20	161.11	99.02	0.98
6.	290	1100	90	20	146.46	99.60	0.40
7.	290	1300	120	20	92.95	99.23	0.77
8.	290	700	110	20	188.31	99.34	0.66
9.	320	900	110	20	161.62	99.06	0.94
10.	320	1100	120	20	121.21	98.68	1.32
11.	320	1300	90	20	136.75	98.92	1.08
12.	320	700	100	20	228.57	98.93	1.07
13.	350	900	120	20	162.04	98.69	1.31
14.	350	1100	110	20	144.63	99.47	0.53
15.	350	1300	100	20	134.62	99.82	0.18
16.	350	700	90	20	277.78	99.48	0.52
17.	400	1500	105	20	126.98	99.40	0.60
18.	150	1200	120	20	52.08	99.00	1.00
19.	350	600	150	20	194.44	99.89	0.11
20.	300	1800	90	20	92.59	100	0
21.	200	2100	75	20	63.49	99.31	0.69
22.	250	900	135	20	102.88	100	0
23.	100	300	60	20	277.78	99.69	0.31
24.	150	2100	90	30	26.46	86.55	13.45
25.	250	1800	105	30	44.09	97.77	2.23
26.	350	1500	120	30	64.81	99.38	0.62
27.	100	1200	135	30	20.58	79.89	20.11
28.	400	300	75	30	592.59	98.93	1.07
29.	200	900	150	30	49.38	94.02	5.98
30.	300	600	60	30	277.78	99.08	0.92
31.	150	900	60	40	69.44	99.12	0.88
32.	100	2100	105	40	11.34	77.74	22.26
33.	350	300	90	40	324.07	96.83	3.17
34.	250	600	75	40	138.89	100	0
35.	300	1500	135	40	37.04	94.06	5.94
36.	200	1800	120	40	23.15	85.71	14.29
37.	400	1200	150	40	55.56	99.91	0.09
38.	400	2100	120	50	31.75	96.32	3.68
39.	250	1500	150	50	22.22	90.25	9.75
40.	100	900	75	50	29.63	92.45	7.55
41.	350	1200	60	50	97.22	99.03	0.97
42.	150	1800	135	50	12.35	79.80	20.20
43.	300	300	105	50	190.48	98.43	1.57
44.	200	600	90	50	74.07	100	0
45.	350	2100	135	60	20.58	87.11	12.89
46.	150	600	105	60	39.68	90.22	9.78
47.	200	1500	60	60	37.04	89.33	10.67
48.	300	1200	75	60	55.56	75.27	24.73
49.	100	1800	150	60	6.17	NA	NA
50.	250	300	120	60	115.74	98.06	1.94
51.	400	900	90	60	82.30	96.11	3.89
52.	400	1800	60	70	52.91	93.37	6.63
53.	150	1500	75	70	19.05	51.70	48.30
54.	350	900	105	70	52.91	96.22	3.78
55.	250	1200	90	70	33.07	89.89	10.11
56.	200	300	135	70	70.55	94.73	5.27
57.	100	600	120	70	19.84	84.70	15.30
58.	300	2100	150	70	13.61	79.86	20.14
59.	250	2100	60	80	24.80	93.81	6.19
60.	350	1800	75	80	32.41	95.56	4.44
61.	400	600	135	80	61.73	98.81	1.19
62.	150	300	150	80	41.67	96.28	3.72
63.	200	1200	105	80	19.84	91.88	8.12
64.	300	900	120	80	34.72	98.76	1.24
65.	100	1500	90	80	9.26	91.92	8.08

(Note: “NA” means no bulk sample formed because lowest energy density cannot melt powder, and after laser processing, it still remains a powder state)

References

[1] Yap CY, Chua CK, Dong ZL. An effective analytical model of selective laser melting. Virtual Phys Prototyp 2016;11:21–6. https://doi.org/10.1080/17452759.2015.1133217.

[2] Tan JH, Wong WLE, Dalgarno KW. An overview of powder granulometry on feedstock and part performance in the selective laser melting process. Addit Manuf 2017;18:228–55. https://doi.org/10.1016/j.addma.2017.10.011.

[3] Martin JH, Yahata BD, Hundley JM, Mayer JA, Schaedler TA, Pollock TM. 3D printing of high-strength aluminium alloys. Nature 2017;549:365–9. https://doi.org/10.1038/nature23894.

[4] Tammas-Williams S, Withers PJ, Todd I, Prangnell PB. The Influence of Porosity on Fatigue Crack Initiation in Additively Manufactured Titanium Components. Sci Rep 2017;7:1–13. https://doi.org/10.1038/s41598-017-06504-5.

[5] Cunningham R, Zhao C, Parab N, Kantzos C, Pauza J, Fezzaa K, et al. Keyhole threshold and morphology in laser melting revealed by ultrahigh-speed x-ray imaging. Science 2019;363:849–52. https://doi.org/10.1126/science.aav4687.

[6] Yap CY, Chua CK, Dong ZL, Liu ZH, Zhang DQ, Loh LE, et al. Review of selective laser melting: Materials and applications. Appl Phys Rev 2015;2:1–21. https://doi.org/10.1063/1.4935926.

[7] Sun D, Gu D, Lin K, Ma J, Chen W, Huang J, et al. Selective laser melting of titanium parts: Influence of laser process parameters on macro- and microstructures and tensile property. Powder Technol 2019;342:371–9. https://doi.org/10.1016/j.powtec.2018.09.090.

[8] Bai Y, Yang Y, Wang D, Zhang M. Influence mechanism of parameters process and mechanical properties evolution mechanism of maraging steel 300 by selective laser melting. Mater Sci Eng A 2017;703:116–23. https://doi.org/10.1016/j.msea.2017.06.033.

[9] Bakhtiarian M, Omidvar H, Mashhuriazar A, Sajuri Z, Gur CH. The effects of SLM process parameters on the relative density and hardness of austenitic stainless steel 316L. J Mater Res Technol 2024;29:1616–29. https://doi.org/10.1016/j.jmrt.2024.01.237.

[10] Paul MJ, Liu Q, Best JP, Li X, Kruzic JJ, Ramamurty U, et al. Fracture resistance of AlSi10Mg fabricated by laser powder bed fusion. Acta Mater 2021;211:116869. https://doi.org/10.1016/j.actamat.2021.116869.

[11] Wu W, Tor SB, Chua CK, Leong KF, Merchant A. Investigation on processing of ASTM A131 Eh36 high tensile strength steel using selective laser melting. Virtual Phys Prototyp 2015;10:187–93. https://doi.org/10.1080/17452759.2015.1106091.

[12] Kim WR, Bang GB, Park JH, Lee TW, Lee BS, Yang SM, et al. Microstructural study on a Fe-10Cu alloy fabricated by selective laser melting for defect-free process optimization based on the energy density. J Mater Res Technol 2020;9:12834–9. https://doi.org/10.1016/j.jmrt.2020.09.051.

[13] Darvish K, Chen ZW, Pasang T. Reducing lack of fusion during selective laser melting of CoCrMo alloy: Effect of laser power on geometrical features of tracks. Mater Des 2016;112:357–66. https://doi.org/10.1016/j.matdes.2016.09.086.

[14] Kasperovich G, Haubrich J, Gussone J, Requena G. Correlation between porosity and processing parameters in TiAl6V4 produced by selective laser melting. Mater Des 2016;105:160–70. https://doi.org/10.1016/j.matdes.2016.05.070.

[15] Agrawal A, Choudhary A. Perspective: Materials informatics and big data: Realization of the “fourth paradigm” of science in materials science. APL Mater 2016;4:1–10. https://doi.org/10.1063/1.4946894.

[16] Xian-meng T, Dong-jian P, Wei C, Xiao-yuan J, Jia-long C, Ze-ming W, et al. Research Progress on Data-Driven Selective Laser Melting Forming Performance Optimization and Intelligent Process Recommendation System. FOUNDRY 2024;73:1487–505.

[17] Su J, Ng WL, An J, Yeong WY, Chua CK, Sing SL. Achieving sustainability by additive manufacturing: a state-of-the-art review and perspectives. Virtual Phys Prototyp 2024;19:1–34. https://doi.org/10.1080/17452759.2024.2438899.

[18] Sing SL, Kuo CN, Shih CT, Ho CC, Chua CK. Perspectives of using machine learning in laser powder bed fusion for metal additive manufacturing. Virtual Phys Prototyp 2021;16:372–86. https://doi.org/10.1080/17452759.2021.1944229.

[19] Wang Z, Yang W, Liu Q, Zhao Y, Liu P, Wu D, et al. Data-driven modeling of process, structure and property in additive manufacturing: A review and future directions. J Manuf Process 2022;77:13–31. https://doi.org/10.1016/j.jmapro.2022.02.053.

[20] Goh GD, Sing SL, Yeong WY. A review on machine learning in 3D printing: applications, potential, and challenges. Artif Intell Rev 2021;54:63–94. https://doi.org/10.1007/s10462-020-09876-9.

[21] Liu Q, Wu H, Paul MJ, He P, Peng Z, Gludovatz B, et al. Machine-learning assisted laser powder bed fusion process optimization for AlSi10Mg: New microstructure description indices and fracture mechanisms. Acta Mater 2020;201:316–28. https://doi.org/10.1016/j.actamat.2020.10.010.

[22] Shevchik SA, Masinelli G, Kenel C, Leinenbach C, Wasmer K. Deep learning for in situ and real-time quality monitoring in additive manufacturing using acoustic emission. IEEE Trans Ind Informatics 2019;15:5194–203. https://doi.org/10.1109/TII.2019.2910524.

[23] Liu B, Fang G, Lei L, Yan X. Predicting the porosity defects in selective laser melting (SLM) by molten pool geometry. Int J Mech Sci 2022;228:107478. https://doi.org/10.1016/j.ijmecsci.2022.107478.

[24] Laleh M, Hughes AE, Yang S, Li J, Xu W, Gibson I, et al. Two and three-dimensional characterisation of localised corrosion affected by lack-of-fusion pores in 316L stainless steel produced by selective laser melting. Corros

Sci 2020;165:108394. https://doi.org/10.1016/j.corsci.2019.108394.

[25] Cunningham R, Narra SP, Montgomery C, Beuth J, Rollett AD. Synchrotron-Based X-ray Microtomography Characterization of the Effect of Processing Variables on Porosity Formation in Laser Power-Bed Additive Manufacturing of Ti-6Al-4V. Jom 2017;69:479–84. https://doi.org/10.1007/s11837-016-2234-1.

[26] Zhao C, Fezzaa K, Cunningham RW, Wen H, De Carlo F, Chen L, et al. Real-time monitoring of laser powder bed fusion process using high-speed X-ray imaging and diffraction. Sci Rep 2017;7:1–11. https://doi.org/10.1038/s41598-017-03761-2.

[27] Zhao C, Parab ND, Li X, Fezzaa K, Tan W, Rollett AD, et al. Critical instability at moving keyhole tip generates porosity in laser melting. Science 2020;370:1080–6. https://doi.org/10.1126/science.abd1587.

[28] Leung CLA, Luczyniec D, Guo E, Marussi S, Atwood RC, Meisnar M, et al. Quantification of Interdependent Dynamics during Laser Additive Manufacturing Using X-Ray Imaging Informed Multi-Physics and Multiphase Simulation. Adv Sci 2022;2203546:1–15. https://doi.org/10.1002/advs.202203546.

[29] Hojjatzadeh SMH, Parab ND, Yan W, Guo Q, Xiong L, Zhao C, et al. Pore elimination mechanisms during 3D printing of metals. Nat Commun 2019;10:1–8. https://doi.org/10.1038/s41467-019-10973-9.

[30] Gong H, Rafi K, Gu H, Starr T, Stucker B. Analysis of defect generation in Ti-6Al-4V parts made using powder bed fusion additive manufacturing processes. Addit Manuf 2014;1:87–98. https://doi.org/10.1016/j.addma.2014.08.002.

[31] Zhao C, Shi B, Chen S, Du D, Sun T, Simonds BJ, et al. Laser melting modes in metal powder bed fusion additive manufacturing. Rev Mod Phys 2022;94:45002. https://doi.org/10.1103/revmodphys.94.045002.

[32] Assuncao E, Williams S, Yapp D. Interaction time and beam diameter effects on the conduction mode limit. Opt Lasers Eng 2012;50:823–8. https://doi.org/10.1016/j.optlaseng.2012.02.001.

[33] Snell R, Tammas-Williams S, Chechik L, Lyle A, Hernández-Nava E, Boig C, et al. Methods for Rapid Pore Classification in Metal Additive Manufacturing. Jom 2020;72:101–9. https://doi.org/10.1007/s11837-019-03761-9.

[34] Laquai R, Müller BR, Kasperovich G, Requena G, Haubrich J, Bruno G. Classification of defect types in SLM Ti-6Al-V4 by X-ray refraction topography. Mater Perform Charact 2020;9:82–93. https://doi.org/10.1520/MPC20190080.

[35] Ji Z, Han Q. A novel image feature descriptor for SLM spattering pattern classification using a consumable camera. Int J Adv Manuf Technol 2020;110:2955–76. https://doi.org/10.1007/s00170-020-05995-3.

[36] Lu C, Shi J, Maitra V. Modelling and process optimization for relative density of Ti6Al4V produced by selective laser melting: a data-driven study. Int J Adv Manuf Technol 2022;121:1973–88. https://doi.org/10.1007/s00170-022-09453-0.

[37] Kusano M, Miyazaki S, Watanabe M, Kishimoto S, Bulgarevich DS, Ono Y, et al. Tensile properties prediction by multiple linear regression analysis for selective laser melted and post heat-treated Ti-6Al-4V with microstructural quantification. Mater Sci Eng A 2020;787:139549. https://doi.org/10.1016/j.msea.2020.139549.

[38] Kamath C. Data mining and statistical inference in selective laser melting. Int J Adv Manuf Technol 2016;86:1659–77. https://doi.org/10.1007/s00170-015-8289-2.

[39] Wang J, Jeong SG, Kim ES, Kim HS, Lee BJ. Material-agnostic machine learning approach enables high relative density in powder bed fusion products. Nat Commun 2023;14:1–12. https://doi.org/10.1038/s41467-023-42319-x.

[40] Box GEP, Lucas HL. Design of Experiments in Non-Linear Situations. Biometrika 1959;46:77–90.

[41] Thenard T, Catapano A, Allena R, El May M, Saintier N, Mesnard M. Topography and wettability characterization of surfaces manufactured by SLM and treated by chemical etching. Mech Adv Mater Struct 2022;29:1674–91. https://doi.org/10.1080/15376494.2020.1836292.

[42] Morse PM. Diatomic Molecules According to the Wave Mechanics. II. Vibrational Levels. Phys Rev 1929;34:57–64.

[43] Lu C, Shi J. Relative density and surface roughness prediction for Inconel 718 by selective laser melting: central composite design and multi-objective optimization. Int J Adv Manuf Technol 2022;119:3931–49. https://doi.org/10.1007/s00170-021-08388-2.

[44] Bai S, Perevoshchikova N, Sha Y, Wu X. The effects of selective laser melting process parameters on relative density of the AlSi10Mg parts and suitable procedures of the archimedes method. Appl Sci 2019;9:1–14. https://doi.org/10.3390/app9030583.

[45] Li J, Kuai Z, Li Z, Liu B, Chen Y, Lu S, et al. Effects of Process Parameters on the Relative Density and Properties of CuCrZr Alloy Produced by Selective Laser Melting. Metals 2022;12:1–13. https://doi.org/10.3390/met12050701.

[46] Huang W, Zhang W, Chen X. Effect of SLM process parameters on relative density of maraging steel (18Ni-300) formed parts. IOP Conf Ser Mater Sci Eng 2020;774. https://doi.org/10.1088/1757-899X/774/1/012027.

[47] Bai Y, Yang Y, Xiao Z, Zhang M, Wang D. Process optimization and mechanical property evolution of AlSiMg0.75 by selective laser melting. Mater Des 2018;140:257–66. https://doi.org/10.1016/j.matdes.2017.11.045.

[48] Lu C, Shi J. Simultaneous consideration of relative density , energy consumption , and build time for selective laser melting of Inconel 718 : A multi-objective optimization study on process parameter selection. J Clean Prod 2022;369:133284.

https://doi.org/10.1016/j.jclepro.2022.133284.
[49] Zhang C, Zhu J, Zheng H, Li H, Liu S, Cheng GJ. A review on microstructures and properties of high entropy alloys manufactured by selective laser melting. Int J Extrem Manuf 2020;2:032003. https://doi.org/10.1088/2631-7990/ab9ead.
[50] Su J, Jiang F, Teng J, Chen L, Yan M, Requena G, et al. Recent innovations in laser additive manufacturing of titanium alloys. Int J Extrem Manuf 2024;6:1–36. https://doi.org/10.1088/2631-7990/ad2545.
[51] Li R, Niu P, Yuan T, Cao P, Chen C, Zhou K. Selective laser melting of an equiatomic CoCrFeMnNi high-entropy alloy: Processability, non-equilibrium microstructure and mechanical property. J Alloys Compd 2018;746:125–34. https://doi.org/10.1016/j.jallcom.2018.02.298.
[52] Li F, Sun Q, Jin P, Liu Y, Chen M, Li J, et al. Wetting behavior of melt and its effect on lack of fusion in arc oscillating NG-GTAW. J Mater Process Technol 2021;296:117176. https://doi.org/10.1016/j.jmatprotec.2021.117176.
[53] Gu D, Guo M, Zhang H, Sun Y, Wang R, Zhang L. Effects of laser scanning strategies on selective laser melting of pure tungsten. Int J Extrem Manuf 2020;2. https://doi.org/10.1088/2631-7990/ab7b00.
[54] Guo M, Gu D, Xi L, Du L, Zhang H, Zhang J. Formation of scanning tracks during Selective Laser Melting (SLM) of pure tungsten powder: Morphology, geometric features and forming mechanisms. Int J Refract Met Hard Mater 2019;79:37–46. https://doi.org/10.1016/j.ijrmhm.2018.11.003.
[55] Khorasani AM, Gibson I, Ghasemi AH, Ghaderi A. A comprehensive study on variability of relative density in selective laser melting of Ti-6Al-4V. Virtual Phys Prototyp 2019;14:349–59. https://doi.org/10.1080/17452759.2019.1614198.
[56] Zhang H, Gu D, Ma C, Xia M, Guo M. Surface wettability and superhydrophobic characteristics of Ni-based nanocomposites fabricated by selective laser melting. Appl Surf Sci 2019;476:151–60. https://doi.org/10.1016/j.apsusc.2019.01.060.
[57] Le-hong T, Lin PC, Chen J, Duc T, Pham Q, Tran X Van. Data-driven models for predictions of geometric characteristics of bead fabricated by selective laser melting. J Intell Manuf 2023;34:1241–57. https://doi.org/10.1007/s10845-021-01845-5.
[58] Saiz E, Tomsia AP, Cannon RM. Ridging effects on wetting and spreading of liquids on solids. Acta Mater 1998;46:2349–61. https://doi.org/10.1016/S1359-6454(98)80016-5.
[59] Ding X, Wang L, Wang S. Comparison study of numerical analysis for heat transfer and fluid flow under two different laser scan pattern during selective laser melting. Optik 2016;127:10898–907. https://doi.org/10.1016/j.ijleo.2016.08.123.
[60] Yu J, Lin X, Wang J, Chen J, Huang W. Mechanics and energy analysis on molten pool spreading during laser solid forming. Appl Surf Sci 2010;256:4612–20. https://doi.org/10.1016/j.apsusc.2010.02.060.
[61] Hu Z, Zhu H, Zhang C, Zhang H, Qi T, Zeng X. Contact angle evolution during selective laser melting. Mater Des 2018;139:304–13. https://doi.org/10.1016/j.matdes.2017.11.002.
[62] Digilov RM. Prediction of surface properties of metals from the law of corresponding states. J Cryst Growth 2003;249:363–71. https://doi.org/10.1016/S0022-0248(02)02072-9.
[63] Hu Z. Study on the Melting and Solidification Behavior of AlCu5MnCdVA Alloy Fabricated by Selective Laser Melting. 2018.
[64] Cai R. Wettability of Fe-TiC and Its Effect on the Properties of TiC/Fe Composites. 2023. https://doi.org/10.26944/d.cnki.gbfju.2023.003164.